

Antisense oligonucleotides selectively enter human-derived antibiotic-resistant bacteria through ATP-binding cassette transporter

Mingzhu Liu

Soochow University

Rong Sun

Soochow university

Jiali Ding

Soochow university

Han Ye

Department of Ophthalmology and Vision Science, Eye, Ear, Nose and Throat Hospital, Fudan University

Binbin Chu

Soochow university

Yunmin Yang

Soochow university

Yuqi Wu

Soochow university

Haoliang Shi

Soochow university

Bin Song

Soochow university

Jiaxu Hong

Department of Ophthalmology and Vision Science, Eye, Ear, Nose and Throat Hospital, Fudan University

Houyu Wang

Soochow university <https://orcid.org/0000-0002-5134-9881>

Yao He (✉ yaohe@suda.edu.cn)

Soochow University <https://orcid.org/0000-0003-1672-4057>

Article

Keywords:

Posted Date: February 10th, 2022

DOI: <https://doi.org/10.21203/rs.3.rs-1336720/v1>

License:  This work is licensed under a Creative Commons Attribution 4.0 International License.

[Read Full License](#)

Abstract

The current vehicles used to deliver antisense oligonucleotides (ASOs) cannot distinguish between bacterial and mammalian cells, greatly hindering the preclinical or clinical treatment of bacterial infections, especially those caused by antibiotic-resistant bacteria. Herein, we leverage bacteria-specific ATP-binding cassette (ABC) transporters to selectively internalize ASOs by hitchhiking them on the unique carbon source of bacterial cells. Compared with their cell-penetrating peptide counterparts, which are non-specifically engulfed by both mammalian and bacterial cells and which display a low uptake rate (i.e. 14.7%), the presented therapeutics consisting of glucose polymer and antisense peptide nucleic acid-modified nanoparticles are selectively internalized into the human-derived multidrug-resistant *Escherichia coli* and methicillin-resistant *Staphylococcus aureus*, and they display a much higher uptake rate (i.e. 51.6%). We demonstrate that the developed strategy allows specific and efficient killing of nearly 100% of the antibiotic-resistant bacteria. We also show its significant curative efficacy against bacterial keratitis and endophthalmitis in mice. This strategy will expand the focus of antisense technology to include bacterial cells other than mammalian cells.

Full Text

To save precious time in the clinic, physicians generally prescribe broad-spectrum antibiotics to patients before an accurate diagnosis is obtained. However, the scattergun overuse of antibiotics tends to promote the emergence of antibiotic-resistant (ABR) bacteria. Moreover, broad-spectrum antibiotics kill not only pathogenic bacteria, but also beneficial bacteria¹⁻³. Meanwhile, CRISPR-Cas therapy, engineered toxins and stapled antimicrobial peptides have recently emerged as targeted and effective antimicrobials⁴⁻⁹. Unlike these antimicrobials, antisense oligonucleotides (ASOs) can target specific bacterial genes and inhibit transcription through complementary base pairing, significantly expanding the available therapeutic targets, even in ABR bacteria¹⁰⁻¹⁶. Of note, the prerequisite for the binding of ASOs to their complementary genes is their delivery into bacterial cells. However, due to the electrostatic charge or size barriers imposed by the unique bacterial plasma membrane and cell wall, it is difficult for pristine ASOs to freely enter bacterial cells¹⁷⁻¹⁹. Such a process generally requires the conjugation of ASO cargo to vectors; however, the current vehicles used to deliver ASOs cannot discriminate between bacterial and mammalian cells. Thus far, efforts to develop antisense technology have focused on mammalian cells rather than on bacterial cells^{10,20,21}. Since the discovery of the bacteria-specific ATP-binding cassette (ABC) transporter, three decades of groundbreaking research have elucidated the mechanisms of the selective internalization of carbohydrates (e.g. amylose, starch, maltodextrin, and maltose) into bacterial cells²²⁻²⁸, but these insights have not yielded ABC transporter-based strategies successful in delivering ASOs into bacterial cells.

We set out to selectively deliver ASOs into bacteria, including human-derived ABR bacteria (e.g. multidrug-resistant (MDR) *Escherichia coli* and methicillin-resistant *Staphylococcus aureus* (MRSA)), by hitchhiking them on carbohydrates (**Fig. 1a**). In the developed strategy, both Gram-negative and Gram-positive

bacteria robustly and selectively ‘eat’ their counterfeiting ‘foods’, that is, glucose polymer (GP) and antisense peptide nucleic acid (asPNA)-modified fluorescent silicon nanoparticles (SiNPs) (GP-SiNPs-asPNA). **Supplementary Fig. 1** showed the synthetic route for GP-SiNPs-asPNA. Typically, the aldehyde groups of the GP molecules (e.g. poly[4-O-(α -D-glucopyranosyl)-D-glucopyranose]) were reacted with the amino groups on the surface of SiNPs to form a stable structure (GP-SiNPs) based on the Schiff base reaction²⁹. Subsequently, Cy7.5-labeled asPNA (see the detailed sequences in **Supplementary Table 1** and related characterizations of HPLC and mass spectrometry in **Supplementary Fig. 2**) was covalently linked to GP-SiNPs via an EDC/NHS condensation reaction between the amino groups of Glu in asPNA and the carboxyl groups on the surface of the SiNPs. The GP-SiNPs-asPNA entered the bacterial intracellular volume through the bacteria-specific ABC transporter pathway (**Fig. 1a**). Unlike CPP-conjugated asPNA (e.g. KFFKFFKFFK-asPNA ((KFF)₃K-asPNA)), which could enter both mammalian and bacterial cells, GP-SiNPs-asPNA could hardly enter mammalian cells due to the absence of ABC transporters on the cell membrane of mammalian cells. As shown in **Fig. 1b**, the ABC transporter in *E. coli* basically consisted of five subunits: (1) LamB, the outer membrane diffusion porin; (2) MalE, the major recognition site for α (1-4)-glucosidically linked glucose polymer; (3) MalF and (4) MalG, two tightly membrane-bound permease subunits; and (5) MalK, the ATP-hydrolyzing subunit of the transporter³⁰⁻³⁴.

The GP-SiNPs-asPNA and free SiNPs (**Supplementary Fig. 3**) in the transmission electron micrograph (TEM) images all displayed spherical shapes with good monodispersity. Dynamic light scattering (DLS) measurements (**Supplementary Fig. 4**) revealed that the hydrodynamic diameter of GP-SiNPs-asPNA (e.g. ~3.62 nm) was slightly larger than that of free SiNPs (e.g. ~5.62 nm). To assess whether the small-sized GP-SiNPs-asPNA could enter bacterial cells, we first performed scanning electron microscopy (SEM) and high-angle annular dark field-scanning TEM (HAADF-STEM). The MDR *E. coli* and MRSA cells isolated from patients with keratitis were treated with GP-SiNPs-asPNA at 37 °C for 2 h, followed by washing with PBS buffer several times. As revealed in the SEM images in **Fig. 1c**, the surface and morphology of the GP-SiNPs-asPNA treated bacteria were not distinctly different from those of the untreated bacteria. As further shown in the HAADF-STEM data (**Fig. 1d**), silicon elements existed only in the GP-SiNPs-asPNA-treated bacteria and not in the untreated bacteria. These results demonstrate that the bacteria indeed engulfed the GP-SiNPs-asPNA.

To facilitate gene therapy, asPNA consisted of two consequent blocks: Ec108 *acpP* and Sau101 *fmbB*. After being internalized into the intracellular volume of *E. coli*, the Ec108 *acpP* block would complement its target, the messenger RNA of Ec108 *acpP* (mEc108 *acpP*), inhibiting the synthesis of fatty acids³⁵⁻³⁷. Analogously, when GP-SiNPs-asPNA entered the *S. aureus* cells, the Sau101 *fmbB* block would combine with the messenger RNA of Sau101 *fmbB* (mSau101 *fmbB*), preventing the synthesis of peptidoglycan^{38,39}. To confirm this antimicrobial mechanism, we extracted RNA from an equal number of MDR *E. coli* or MRSA incubated with GP-SiNPs-asPNA at various concentrations (i.e. 250 nM, 500 nM and 1 μ M). The extracted RNA was analysed by semiquantitative PCR and qPCR; 16S cDNA amplified by primers was used as control. The corresponding primer sequences are shown in **Supplementary Table 2**. Expectedly, we found that GP-SiNPs-asPNA inhibited the expression of both *acpP* in MDR *E. coli* (**Fig.**

1e) and *fmhB* in MRSA (**Fig. 1f**). Moreover, the expression levels of both *acpP* and *fmhB* decreased as the GP-SiNPs-asPNA concentration increased, indicating a concentration–response strategy. The PCR results also indirectly demonstrated the internalization of GP-SiNPs-asPNA into bacterial cells.

The UV-vis absorption spectrum of GP-SiNPs-asPNA in **Supplementary Fig. 5a** showed two characteristic peaks at 320 nm (assigned to SiNPs) and 788 nm (assigned to Cy7.5). Accordingly, we observed two typical photoluminescence (PL) peaks located at 520 nm (excitation at 405 nm) and 808 nm (excitation at 808 nm), which were assigned to SiNPs and Cy7.5, respectively (**Supplementary Fig. 6**). By leveraging the emission properties of GP-SiNPs-asPNA, we next used confocal laser scanning microscopy (CLSM) to image the bacteria treated with asPNA, SiNPs-asPNA, GP-SiNPs-asPNA and (KFF)₃K-asPNA (Cy7.5 labeled) at equivalent doses at 37 °C for 2 h, followed by washing with PBS buffer several times. The detailed sequence of (KFF)₃K-asPNA and related characterizations were shown in **Supplementary Table 1 and Supplementary Fig. 7**. To test whether GP-SiNPs-asPNA could specifically target diverse bacteria, we first selected four representative bacteria, i.e., Gram-negative bacteria of *E. coli* and *P. aeruginosa* and Gram-positive bacteria of *S. aureus* and *M. luteus* as targets. As revealed in **Fig. 2a**, green fluorescent signals (assigned to SiNPs, first column, $\lambda_{\text{ex}} = 405 \text{ nm}$, $\lambda_{\text{em}} = 500\text{-}550 \text{ nm}$) and red fluorescent signals (assigned to Cy7.5, $\lambda_{\text{ex}} = 633 \text{ nm}$, $\lambda_{\text{em}} = 700\text{-}800 \text{ nm}$) were barely detectable in either the asPNA or SiNP-asPNA groups. Additionally, weak red fluorescent signals were detectable in (KFF)₃K-asPNA-treated *E. coli* and *P. aeruginosa*, while they were hardly detectable in (KFF)₃K-asPNA-treated *S. aureus* and *M. luteus*, in agreement with the reported result that CPPs-asPNA more easily enter Gram-negative bacteria than Gram-positive bacteria^{19,40,41}. In contrast, we observed very strong green and red fluorescent signals in all GP-SiNPs-asPNA treated bacteria. Furthermore, green fluorescence overlapped well with red fluorescence in the merged channel in the GP-SiNPs-asPNA groups. Importantly, we observed the identical results in GP-SiNPs-asPNA treated MRSA and MDR *E. coli* isolated from patients with keratitis (**Fig. 2b**). The human-derived strains were obtained from patients with keratitis who were diagnosed and treated in the Shanghai Eye, Ear, Nose and Throat Hospital, Fudan University. The corresponding histograms of fluorescent intensity in **Fig. 2c** further revealed that the red fluorescent signals observed in GP-SiNPs-asPNA groups were significantly higher than those in (KFF)₃K-asPNA groups ($p < 0.001$). These results primarily verified the bacteria-targeting ability of GP molecules.

Upon the addition of phenol-sulfuric acid, the UV-vis absorption spectrum of GP-SiNPs-asPNA exhibited a new peak at 490 nm, assigned to furfural resin, which was produced by the reaction between GP and phenol (**Supplementary Fig. 5b**). We determined the amounts of linked GP and Cy7.5-asPNA through the corresponding calibration absorption curves (**Supplementary Fig. 8**). Typically, when the reaction concentration of asPNA was 1 μM , the loading rate reached $\sim 53\%$. To investigate the effect of the amount of linked GPs and incubation time on the uptake efficiency of GP-SiNPs-asPNA by bacteria, we performed dose- and time-response experiments by using CLSM. Typically, $\sim 1.0 \times 10^9$ CFU of *E. coli* or *S. aureus* were incubated with GP-SiNPs-asPNA containing GP at various concentrations (e.g., 0, 2.5, 5, 10 and 15 mg mL^{-1}) for 0.5 h, 1 h, 1.5 h, 2 h and 2.5 h, respectively. As shown in **Supplementary Fig. 9**, the fluorescent signal became stronger when GP concentration and incubation time increased, suggesting

that the uptake of GP-SiNPs-asPNA by bacterial cells was dose- and time-dependent. Typically, when the GP concentration was 10 mg mL^{-1} and the incubation time was 2 h, the fluorescence signal reached its peak. If further enhancing the GP concentration and the incubation time, the fluorescence signal did not improve significantly. Quantitatively, the uptake rate of GP-SiNPs-asPNA by bacteria after 2 h of incubation was further analyzed by flow cytometry. Consistent with the results in **Supplementary Fig. 9**, the uptake rate of GP-SiNPs-asPNA (2.5 mg mL^{-1} GP) by *E. coli* was 15.2% and that by *S. aureus* was 16.9%, and the uptake rate of GP-SiNPs-asPNA (10 mg mL^{-1} GP) by *E. coli* climbed to 52.8% and that by *S. aureus* was 56.4% (**Fig. 2d**). When the GP concentration reached 15 mg mL^{-1} , the uptake rate of GP-SiNPs-asPNA by *E. coli* was 54.5% and that by *S. aureus* was 59.4%, with a tiny increase, indicating that a relative GP saturation state was achieved. As such, 10 mg/mL GP and 2-h incubation were employed in the following experiments. Comparatively, when loading the same amount of asPNA (e.g., $1 \mu\text{M}$), the uptake rate of $(\text{KFF})_3\text{K}$ -asPNA by *E. coli* was only 21.1% and that by *S. aureus* was only 9.97% after 2 h of incubation, which was much lower than that of GP-SiNPs-asPNA. Likewise, the uptake rate of GP-SiNPs-asPNA by MDR *E. coli* was 45.6% and that by MRSA was 51.6%; while the uptake rate of $(\text{KFF})_3\text{K}$ -asPNA by MDR *E. coli* was only 14.7% and that by MRSA was only 17.5%.

To examine the selectivity of GP-SiNPs-asPNA towards bacteria over mammalian cells, human retinal pigment epithelial cells (ARPE-19) spiked with MDR *E. coli* or MRSA were incubated with GP-SiNPs-asPNA or $(\text{KFF})_3\text{K}$ -asPNA for 2 h and then washed with PBS buffer. As shown in **Fig. 2e**, we observed green and red fluorescent signals only in bacteria rather than in ARPE-19 cells in the GP-SiNPs-asPNA group. In contrast, in the $(\text{KFF})_3\text{K}$ -asPNA-treated groups, red fluorescence signals were detectable in both ARPE-19 cells and bacterial cells. In human blood samples spiked with *E. coli* or *S. aureus* under the same treatments, we observed similar phenomena (**Supplementary Fig. 10**). Collectively, these results confirmed that the developed strategy featured higher selectivity towards bacteria over mammalian cells than $(\text{KFF})_3\text{K}$ -asPNA.

Ultimately, the transport mechanism of GP-SiNPs-asPNA into bacteria was systematically investigated based on inhibition assays and competition assays. As shown in the inhibition assay in **Fig. 2f**, we did not observe any fluorescent signals in sodium azide (NaN_3)- and GP-SiNPs-asPNA treated bacteria in which NaN_3 , serving as a bacterial respiratory inhibitor, could inhibit the work of ABC transporter⁴². As shown in the competition assay in **Fig. 2g**, the fluorescent signals of GP-SiNPs-asPNA in *E. coli* gradually decreased when the bacteria were pretreated with GP at increasing concentrations (e.g., 0, 2 and 20 mg mL^{-1}). These results together demonstrated that the internalization of nanoprobe into bacterial cells was based on the ABC transporter pathway.

We used the agar plate assay to intuitively evaluate the antimicrobial activity of the proposed strategy *in vitro* (**Fig. 3a**). In order to highlight the superiority of this strategy, the direct comparison with the clinically used antibiotics was performed, including ciprofloxacin, norfloxacin and ampicillin. As expected, compared to PBS groups, we found slightly fewer MDR *E. coli* colonies, and almost no *P. aeruginosa* or *M. luteus* colonies in the ciprofloxacin, norfloxacin or ampicillin groups. This suggested that even broad-

spectrum antibiotics at the high dose of $15 \mu\text{g mL}^{-1}$ featured limited therapeutic effects against the human-derived MDR *E. coli*. Although they were not effective at killing MDR *E. coli*, they indiscriminately killed the non-resistant bacteria, e.g., *P. aeruginosa* or *M. luteus*. Also, we observed numerous *MRSA* colonies in ampicillin treated group. In the GP-SiNPs-asPNA groups, we observed nearly no MDR *E. coli* or *MRSA* colonies, corresponding to a much lower bacterial count; while numerous *P. aeruginosa* or *M. luteus* colonies, corresponding to a large amount of bacterial count (**Fig. 3b**). As further revealed in **Fig. 3c**, the presented strategy showed dominant antibacterial rates against *MRSA* ($\sim 99.99\%$) and MDR *E. coli* ($\sim 99.99\%$) but displayed almost no therapeutic effects against *P. aeruginosa* or *M. luteus*. On the contrary, other antibiotics even at $15 \mu\text{g mL}^{-1}$ displayed inferior antibacterial rates against MDR *E. coli* (e.g., ciprofloxacin: $\sim 60.51\%$, norfloxacin: $\sim 75.92\%$; ampicillin: 56.04%) but distinct therapeutic effects against *P. aeruginosa* or *M. luteus* (e.g., $>99\%$). The results of semiquantitative PCR and qPCR further demonstrated that GP-SiNPs-asPNA specifically inhibited the expression of target genes (**Supplementary Fig. 11**). These results demonstrated that the developed strategy could selectively and efficiently kill antibiotic-resistant bacteria. We also employed the established methylthiazole tetrazolium (MTT) method to evaluate the cytotoxicity of GP-SiNPs-asPNA towards mammalian cells, including mouse retinal endothelial cells (MRECs) and ARPE-19 cells. As shown in **Supplementary Fig. 12**, the cell morphology of both MRECs and ARPE-19 cells did not change significantly, and the cell viability remained above 90% even when the concentration of GP-SiNPs-asPNA was up to $1 \mu\text{M}$. These results indicated the negligible cytotoxicity of GP-SiNPs-asPNA towards ocular cells. Additionally, GP-SiNPs-asPNA showed good stability after 7 days of storage in PBS or 10% fetal bovine serum (FBS) (**Supplementary Fig. 13**), implying its promising applications *in vivo*.

As for *in vivo* applications, we chose ocular bacterial infections as targets. Due to tear clearance and frequent blinking, the efficiency of conventional antibiotics for eye infections by using topical administration is usually less than 5%⁴³⁻⁴⁵. Therefore, the administration of antibiotics at high doses is generally performed multiple times a day for severe cases. Intense antibiotics therapy is prone to the generation of an increasing number of clinically resistant pathogens, especially superbugs. We established bacterial keratitis and endophthalmitis models in mice. To construct bacterial keratitis models, Sprague–Dawley (SD) mice (female, 6-8 weeks, $n=5$) were first anesthetized, followed by scratching 4 scars with the same depth and size on the cornea by using a sterile knife. Then, $200 \mu\text{L}$ of *E. coli*, *S. aureus* or the mixture of *E. coli* and *S. aureus* (*E. coli*+*S. aureus*) with various concentrations was dropped onto the corneas. After one day of infection with bacteria, the corneas were dropped with SiNPs, SiNPs-asPNA, vancomycin-modified SiNPs (SiNPs-Van) or GP-SiNPs-asPNA at the equivalent dose for 5 days (one drop per time ($\sim 20 \mu\text{L}$), three times per day) (**Fig. 4a**). The dropped agents were kept on the corneal surface for 30 min and then washed with PBS. **Supplementary Fig. 14** illustrated the construction of bacterial endophthalmitis models (*E. coli* + *S. aureus*, $\sim 3.0 \times 10^6$ CFU) in mice. For treating the mice with bacterial endophthalmitis, we added poloxamer 407 (P407) to GP-SiNPs-asPNA solution, followed by dropping on corneas. Gelation of the mixed solution was rapidly achieved, prolonging drug retention on the ocular surface. As revealed in the drug release curves in **Supplementary Fig. 15**, the 25% gel formulation displayed the slowest drug release (e.g., 50% drug release rate after 40 min, 71% drug release

rate after 2 hours). **Supplementary Fig. 16** revealed the red fluorescence from GP-SiNPs-asPNA could be observed in the external retina, suggesting that GP-SiNPs-asPNA could enter the inside of the eyeball.

In the bacterial keratitis models, we used a fluorescence stereoscopic microscope (Olympus, SZX16, $\lambda_{\text{ex}} = 488 \text{ nm}$) to capture the fluorescent images of infected corneas after first drug administration (**Fig. 4b**). The actual count of *E. coli* or *S. aureus* at the infected cornea during imaging was determined by tissue harvesting, homogenization and culturing with CFU count. As expected, no fluorescent signals could be detectable in the PBS, asPNA or SiNPs-asPNA groups. Indeed, SiNPs-Van could image *S. aureus* keratitis, while they could not image *E. coli* keratitis owing to the strong affinity between vancomycin and the D-Ala-D-Ala moiety in the cell wall of *S. aureus*⁴⁶. As further supported by the corresponding histograms, *S. aureus*-infected corneas treated with SiNPs-Van had an ~16.4-fold increase in fluorescence intensity compared with *E. coli*-infected corneas treated with SiNPs-Van. In contrast, we observed green fluorescence signals in both *E. coli*- and *S. aureus*-infected corneas, indicating that the proposed hitchhiking strategy allowed imaging of diverse bacterial keratitis. Additionally, we were eager to image keratitis caused by diverse bacteria at various concentrations to determine the detection threshold of the developed strategy. Typically, when the *E. coli* or *S. aureus* concentration during imaging decreased from $\sim 1.0 \times 10^6$ to $\sim 1.0 \times 10^4$ CFU, the corresponding fluorescence signal became weak, suggesting the bacterial concentration-dependent manner of the hitchhiking strategy. As revealed in the corresponding histograms, even though the *S. aureus* concentration during imaging was as low as $\sim 1.0 \times 10^4$ CFU, the GP-SiNPs-asPNA treated cornea had an ~3.62-fold enhancement in fluorescence intensity compared with the SiNPs-Van group. In this case, SiNPs-Van targeted the bacterial cell wall and was unable to access the bacterial intracellular volume. As a consequence, the payloads of GP-SiNPs-asPNA internalized into the intracellular volume of bacteria were relatively higher than those of SiNPs-Van on the bacterial cell wall, leading to a better detection sensitivity. Such ultrahigh sensitivity was approximately three orders of magnitude higher than most contrast agents, which should be sufficient for many *in vivo* scenarios⁴⁷.

We used a slit-lamp microscope to observe the daily corneal changes during the treatment. As shown in **Fig. 4c**, clearly visible corneas were observed at the beginning (0 d). After one day of infection, each group had mild corneal edema, mild iris hyperaemia and a small amount of secretion. After five days of treatment, these symptoms were increasingly relieved in GP-SiNPs-asPNA groups and *S. aureus* keratitis treated with SiNPs-Van. In contrast, these signs worsened in the other groups. Specifically, on the fifth day of treatment, corneas returned to normal in the GP-SiNPs-asPNA groups, while the corneas in the PBS, SiNPs and SiNPs-asPNA groups were completely cloudy and severely congested, featuring severe corneal stroma edema and unclear iris texture. As further evaluated by slit-lamp microscope in **Fig. 4d**, on average, the corneal opacity scores in the GP-SiNPs-asPNA group gradually decreased. Similarly, the scores in *S. aureus* keratitis mice treated with SiNPs-Van gradually decreased. In contrast, the scores in other groups gradually increased. In the bacterial endophthalmitis models, as shown in **Supplementary Fig. 17**, one day after infection, the pupils in all groups appeared opaque, and the eyes were congested and swollen. After one day of treatment, the pupils only in the GP-SiNPs-asPNA gel system were slightly

relieved, while the inflammation symptoms worsened in the other groups. Specifically, after four days of treatment, we observed only mild inflammation in the GP-SiNPs-asPNA gel system, while the pupils were yellow and cloudy, with considerable hyperaemia and secretion, and the eyeballs were severely damaged in the other groups. We also used the slit-lamp microscope to evaluate the effects of GP-SiNPs-asPNA on the corneas of healthy mice. After 5-day topical administration, the corneas in each group were clearly visible, without swelling or unknown secretions (**Supplementary Fig. 18**).

The daily corneal colony of each group was given in **Figs. 4e & 4f**. Typically, the number of bacterial colonies in the GP-SiNPs-asPNA group continued to decrease over time. Additionally, the number of *S. aureus* colonies in the SiNPs-Van group decreased over time. In contrast, the number of bacterial colonies in other groups increased over time. Accordingly, the *in vivo* bacteriostatic rate of GP-SiNPs-asPNA on keratitis was calculated to be 99% against *E. coli* and 99% against *S. aureus*, 98.6% against *E. coli* + *S. aureus*. The bacteriostatic rate of SiNPs-Van on keratitis was calculated to be 98% against *S. aureus*. In the bacterial endophthalmitis models, the bacteriostatic rate of GP-SiNPs-asPNA on endophthalmitis caused by *E. coli* + *S. aureus* was calculated to be 98.8% supported by agar plate assays, in which eyeball homogenates were cultured to obtain bacterial colonies (**Supplementary Fig. 19**). Ultimately, to histologically analyze the inflammation of the infected cornea after the treatment, hematoxylin-eosin (H&E) staining was performed (**Fig. 4g**). Consistently, we observed almost no inflammatory cell infiltrates in bacteria-infected corneal tissues treated with GP-SiNPs-asPNA and *S. aureus*-infected corneal tissues treated with SiNPs-Van. In contrast, we found a large number of inflammatory cell infiltrates in other groups. We also observed the similar results in H&E staining of the retinal membrane in the bacterial endophthalmitis models (**Supplementary Fig. 20**). As shown by H&E staining of eyeball sections of healthy mice treated with GP-SiNPs-asPNA in **Supplementary Fig. 21**, we observed no significant changes in the morphology of corneal tissues and retinal tissues among the groups, suggesting negligible toxicity of GP-SiNPs-asPNA *in vivo*. Collectively, these evidences fully proved that the hitchhiking strategy featured excellent therapeutic effects on ocular infections in mice caused by diverse bacteria.

Methods

Chemicals, reagents and bacteria. The *poly[4-O-(α -D-glucopyranosyl)-D-glucopyranosyl]*, (3-aminopropyl) trimethoxysilane, 1,8-naphthalimide, N-(3-dimethylaminopropyl)-N'-ethylcarbodiimide hydrochloride (EDC), N-hydroxysulfosuccinimide (NHS), NaBH₄ and vancomycin were obtained from Sigma-Aldrich (Shanghai, China). The Cy7.5-labelled asPNA was purchased from Hangzhou Tahoe Biotechnology Co., Ltd. Bacterial culture reagents (LB medium) were obtained from Sangon Biotech (Shanghai, China), and cell culture reagents were purchased from Gibco (Grand Island, USA). The *E. coli* (ATCC 11303), *S. aureus*, *M. luteus* (BNCC 102589), *P. aeruginosa* (BNCC 125486), ARPE-19 and MREC cells were purchased from BeNa Culture Collection (BNCC, Shanghai, China). Human blood samples were provided by a healthy male volunteer. Human-derived MRSA and MRD *E. coli* were isolated from patients with keratitis and were supplied by the Eye Bank of the Eye, Ear, Nose and Throat Hospital, Fudan University, under the approval

of the hospital ethics committee (EENTIRB-2017-06-07-01). Experiments were conducted according to the Declaration of Helsinki and in compliance with Chinese law.

The synthesis of GP-SiNPs-asPNA. To synthesize fluorescent SiNPs, (3-aminopropyl) trimethoxysilane was mixed with 1,8-naphthimide molecules and was irradiated with 365 nm ultraviolet light in a dark environment for 40 min, followed by centrifugation for 15 min (6000 rpm) and ultrafiltration (MWCO, 1000, Spectra/Pro) in deionized water to remove residues. The as-resultant SiNPs solution was stored in darkness at 4 °C. To synthesize GP-SiNPs, *poly[4-O-(α -D-glucopyranosyl)-D-glucopyranosyl]* solution (100 μ l, 10 mg mL⁻¹) was reacted with SiNPs solution (150 μ l, 25 mg mL⁻¹) for 6 hours at 70 °C upon addition of NaBH₄ of 0.01mg, followed by centrifugation at 7500 rpm for 15 min to remove unreacted GPs. The Cy7.5-labelled asPNA and cell penetrating peptides of ((KFF)₃K) designed by our laboratory were individually synthesized by solid phase peptide synthesis (SPPS) methodologies and purified by high performance liquid chromatography (HPLC) (Nanchang, China). To synthesize GP-SiNPs-asPNA, asPNA solution (100 μ l, 1000 nmol) was reacted with the as-prepared GP-SiNPs solution (25 μ l) for 12 hours at 4 °C upon addition of EDC solution (50 μ l, 50 mg mL⁻¹) and NHS solution (12.5 μ l, 50 mg mL⁻¹), followed by centrifugation for 15 min (6000 rpm) and ultrafiltration (MWCO, 1000, Spectra/Pro) to remove unreacted asPNA. To synthesize vancomycin modified SiNPs (SiNPs-Van), vancomycin solution (100 μ l, 80 mg/mL) was reacted with SiNPs solution (150 μ l, 25 mg mL⁻¹) for 12 hours at 4 °C upon addition of EDC solution (50 μ l, 50 mg mL⁻¹) and NHS solution (12.5 μ l, 50 mg mL⁻¹), followed by followed by centrifugation for 15 min (6000 rpm) and ultrafiltration (MWCO, 1000, Spectra/Pro) to remove unreacted vancomycin. A transmission electronic microscopy (TEM) (Philips CM 200, 200kV) was employed to characterize the morphology and size of as-prepared nanoagents. The Delsa™ nano submicron particle size analyzer (Beckman Coulter, Inc.) was used to analyze the dynamic light scattering (DLS) of nanoagents. A UV-vis spectrophotometer (Perkin-Elmer lambda) was utilized to measure the UV-vis absorption spectra of nanoagents. A spectro-fluorimeter (HORIBA JOBIN YVON FLUORMAX-4) was used to record photoluminescence (PL) spectra of nanoagents.

***In vitro* imaging of diverse bacteria via the developed strategy.** The lyophilized powders of *E. coli*, *S. aureus*, *M. luteus* and *P. aeruginosa* were respectively dissolved in LB medium. Next, the bacteria dissolved in LB medium were cultured on the LB plate medium at 37 °C for 12 hours to pick a single colony. After that, the picked colony was cultured in LB liquid medium at 250 rpm and 37 °C. Afterwards, the suspensions of bacteria in the exponential growth phase were washed twice and re-suspended in PBS buffer. The optical density (OD) at 600 nm was measured to determine the concentration of bacteria. A colony counting instrument (Czone 8) was used to determine the number of bacterial colonies. MRECs cells were cultured in the Dulbecco's modified Eagle's medium (DMEM) containing high glucose in a humidified incubator with 5% CO₂ at 37 °C. ARPE-19 cells were cultured in Roswell Park Memorial Institute (RPMI)-1640 medium supplemented with 10% heat-inactivated fetal bovine serum (FBS), 100 μ g mL⁻¹ streptomycin and 100 U mL⁻¹ penicillin in a humidified incubator with 5% CO₂ at 37 °C.

The $\sim 1.0 \times 10^9$ CFU *E. coli*, *S. aureus*, *M. luteus* or *P. aeruginosa* was incubated with GP-SiNPs-asPNA (1 μ M, 200 μ L) in a shaking incubator at 200 rpm and 37 °C for 2 hours. Next, the treated bacteria were collected by centrifugation at 6000 rpm for 5 min. Then the collected bacteria were re-suspended and washed with PBS buffer for several times, followed by imaging by a confocal laser scanning microscope (Leica, TCSSP5 II) equipped with 30% power of diode laser. All confocal images were captured under the same brightness and contrast. The commercial image analysis software (Leica Application Suite Advanced Fluorescence Lite) was used to analyze region of interest (ROI). The scanning electron microscopy (SEM) and high-angle annular dark field-scanning TEM (HAADF-STEM) were performed to verify the internalization of GP-SiNPs-asPNA into bacterial cells.

Inhibition of target gene expression in bacteria. GP-SiNPs-asPNA (200 μ L, 1 μ M) incubated with $\sim 1.0 \times 10^9$ CFU *E. coli* or *S. aureus* in a shaking incubator at 200 rpm and 37 °C for 12 hours. After incubation, the bacteria were collected by centrifugation at 8000 rpm for 10 min, then were re-suspended and washed with PBS buffer for several times. We used the RNeasy Plus Mini kit with a genomic DNA eliminator to extract total RNA from the treated bacteria. Then we used the RNase-free water to dissolve the as-extracted RNA, followed by cDNA preparation by using the cDNA synthesis kit. Afterwards, we used the qPCR to amplify each target mRNA. The whole qPCR procedure began with an initial activation step of 94 °C for 3 min, followed by 40 cycles of 94 °C for 5 sec and 60 °C for 34 sec. The primer dimer formation and incorrect priming was examined by a melting curve. 16S cDNA amplified by primers in this case was used as the control. Agarose gel electrophoresis was running at 90 V to analyze the amplified nucleic acids.

***In vivo* imaging of diverse bacteria in mice corneas via the developed strategy.** Approximately 150-200 g Sprague-Dawley (SD) female mice were purchased from Changzhou Kavins Experimental Animal Co., Ltd. All animal experiments were following the protocol approved by the animal care committee of Soochow University. Sprague-Dawley (SD) mice (female, SPF grade, 6-8 weeks old) were feed at 25°C and 65% humidity adjusted by the ventilation equipment and air filtration system. Mice were anesthetized by intraperitoneal injection of 150 μ L of 5% pentobarbital sodium solution, and then intramuscular injection of 50 μ L of 2% xylazine hydrochloride. The eyelid of mice was dragged and the scratched cornea were topically administrated with one drop of 20 μ L of PBS, asPNA (1 μ M), SiNPs-asPNA (1 μ M), SiNPs-Van (10 mg/mL) or GP-SiNPs-asPNA (1 μ M). After that, the cornea was washed with PBS buffer. The infected corneas were imaged by using a fluorescence stereoscopic microscope (Olympus, SZX16, λ_{ex} = 488 nm), and the image was analyzed by the ImageJ software. The actual amount of bacteria at the infection cornea during imaging was determined *via* tissue harvesting, homogenization and culturing with CFU count. The number of bacterial colonies was counted by a colony counting instrument (Czone 8).

Therapy of ocular bacterial infections. The bacterial keratitis model in mice was established by using the scratch method. In details, the scars with the same depth and size were cut on the deep layer of corneal stroma of anesthetized mice by using a sterile scalpel. Afterwards, 200 μ L of bacterial solution ($\sim 1.0 \times 10^9$

CFU) was dropped onto the cornea and held for 15 min. The mice were divided into five groups, and were topically administrated with one drop of 20 μL of PBS, asPNA (1 μM), SiNPs-asPNA (1 μM), SiNPs-Van (10 mg/mL) or GP-SiNPs-asPNA (1 μM), respectively (one drop per time, three times per day). The severity of keratitis was scored based on the cornea images captured by the slit lamp. At the last day of treatment, the bacteria were extracted from the infected cornea and were cultured on the agar plates. The number of bacterial colonies was counted by a colony counting instrument (Czone 8). Meanwhile, the infected tissues from each group were fixed in eyeball fixative and then embedded in paraffin solution for H&E staining. The bacterial endophthalmitis model in mice was established by intravitreal injection. Typically, 3 μL of $\sim 1.0 \times 10^9$ CFU *E. coli* and *S. aureus* was injected into the vitreous cavity of the left eye of mice with a microsyringe, and the needle was removed after holding for 15 seconds. Likewise, the mice were divided into five groups, and the cornea in each group were dropped with one drop of 20 μL of 25% poloxamer 407 (P407) gel solutions containing PBS, asPNA (1 μM), SiNPs-asPNA (1 μM), SiNPs-Van (10 mg/mL) or GP-SiNPs-asPNA (1 μM), respectively (one drop per time, three times per day). Similarly, the mice anterior segment was observed by a slit lamp. Accordingly, the severity of inflammation was scored based on the mice anterior segment photos. At the last day of treatment, the mice in each group were sacrificed and their eyeballs were removed, followed by homogenization and culturing with CFU count. The bacterial colonies were determined by using a colony counting instrument (Czone 8). Other harvested eyeballs were treated with Davidson's solution for 30 min and 30% sucrose overnight for dehydration. DAPI-dyed frozen sections were observed under an confocal laser scanning microscope (Leica, TCSSP5 II). Meanwhile, the infected tissues of eyeballs from each group were fixed in eyeball fixative and then embedded in paraffin solution for H&E staining.

Statistical analysis.

We used one-way ANOVA or the paired two-tailed t test (* means $p < 0.05$, ** means $p < 0.01$, *** means $p < 0.001$, **** means $p < 0.0001$, ns means no significance) for statistical significance testing. We used Origin or GraphPad Prism software to perform the statistical analysis. We used commercial image analysis software (Leica Application Suite Advanced Fluorescence Lite, LAS AF Lite) and ImageJ software (NIH Image; <http://rsbweb.nih.gov/ij/>) to process the region of interest (ROI) in fluorescence images.

Life Science Reporting Summary. Further information on the experimental design is available in the Life Science Reporting Summary.

Data availability. The data that support the findings of this study are available within the paper and its supplementary information.

Declarations

Acknowledgements

The authors acknowledge financial support from the National Natural Science Foundation of China (No. 21825402, 22074101, 81970766 and 82171102), Natural Science Foundation of Jiangsu Province of China (No. BK20191417 and BK20200851), the Shanghai Innovation Development Program (2020-RGZN-02033), the Shanghai Key Clinical Research Program (SHDC2020CR3052B), China Postdoctoral Science Foundation (No. 2021M692347) and Program for Jiangsu Specially Appointed Professors to Professor Yao He, a project funded by the Priority Academic Program Development of Jiangsu Higher Education Institutions (PAPD), 111 Project and Collaborative Innovation Center of Suzhou Nano Science and Technology (NANO-CIC).

Author Contributions

M. Z. L., R. S., J. X. H., J. H., H. Y. W. and Y. H. conceived and designed the research. M. Z. L. and R. S. carried out most of the experiments and analysed the data. J. L. D., B. B. C., Y. M. Y., Y. Q. W., H. Y., H. L. S. and B. S performed additional experiments and characterizations. M. Z. L., J. H., H. Y. W and Y. H wrote the manuscript.

Competing interests

The authors declare no competing financial interests.

Additional information

Supplementary Information is available in the online version of the paper.

Reprints and permissions information is available online at www.nature.com/reprints.

Correspondence and requests for materials should be addressed to J. H., H. Y. W. or Y. H.

Publisher's note: Springer Nature remains neutral with regard to jurisdictional claims in published maps and institutional affiliations.

References

1. Austin A, Lietman T, Rose-Nussbaumer J. Update on the management of infectious keratitis. *Ophthalmology* **124**, 1678-1689 (2017).
2. Hernandez, F., Huang, L., Olson, M. *et al.* Noninvasive imaging of *Staphylococcus aureus* infections with a nuclease-activated probe. *Nat. Med.* **20**, 301-306 (2014).
3. Koskiniemi, S. & Virtanen, P. Selective killing of antibiotic-resistant bacteria from within. *Nature*, **570**, 449–450 (2019).
4. Mourtada, R., Herce, H.D., Yin, D.J. *et al.* Design of stapled antimicrobial peptides that are stable, nontoxic and kill antibiotic-resistant bacteria in mice. *Nat. Biotechnol.* **37**, 1186–1197 (2019).

5. Bikard, D. *et al.* Exploiting CRISPR-Cas nucleases to produce sequencespecific antimicrobials. *Nat. Biotechnol.* **32**, 1146–1150 (2014).
6. Citorik, R. J., Mimee, M. & Lu, T. K. Sequence-specific antimicrobials using efficiently delivered RNA-guided nucleases. *Nat. Biotechnol.* **32**, 1141–1145 (2014).
7. Rodriguez-Pagan, I., Novick, R. P., Ross, H. F., Jiang, D. & Ram, G. Conversion of staphylococcal pathogenicity islands to CRISPR-carrying antibacterial agents that cure infections in mice. *Nat. Biotechnol.* **36**, 971–976 (2018).
8. López-Igual, R., Bernal-Bayard, J., Rodríguez-Patón, A. *et al.* Engineered toxin–intein antimicrobials can selectively target and kill antibiotic-resistant bacteria in mixed populations. *Nat. Biotechnol.* **37**, 755–760 (2019).
9. Chikindas, M. L., Weeks, R., Drider, D., Chistyakov, V. A. & Dicks, L. M. Functions and emerging applications of bacteriocins. *Curr. Opin. Biotech.* **49**, 23–28 (2018).
10. Good L, Awasthi S K, Dryselius R, *et al.* Bactericidal antisense effects of peptide-PNA conjugates. *Nat. Biotechnol.* **19**, 360-364 (2001).
11. Delihias, N., Rokita, S. & Zheng, P. Natural antisense RNA/target RNA interactions: Possible models for antisense oligonucleotide drug design. *Nat. Biotechnol.* **15**, 751-753 (1997).
12. Harth, G., Zamecnik, P. C., Tabatadze, D., *et al.* Hairpin extensions enhance the efficacy of mycolyl transferase-specific antisense oligonucleotides targeting Mycobacterium tuberculosis. *Proc. Natl. Acad. Sci. U S A.* **104**, 7199 (2007).
13. Harth, G., Zamecnik, P. C. & Tang, J. Y. Treatment of mycobacterium tuberculosis with antisense oligonucleotides to glutamine synthetase mRNA inhibits glutamine synthetase activity, formation of the poly-l-glutamate/glutamine cell wall structure, and bacterial replication. *Proc. Natl. Acad. Sci. U S A.* **97**, 418-423 (2000).
14. Wesolowski, D. *et al.* Basicpeptide-morpholino oligomer conjugate that is very effective in killing bacteria by gene-specific and nonspecific modes. *Proc. Natl. Acad. Sci. U S A.* **108**, 16582-16587 (2011).
15. Good, L. & Nielsen, P. Antisense inhibition of gene expression in bacteria by PNA targeted to mRNA. *Nat. Biotechnol.* **16**, 355-358 (1998).
16. Pernitzsch, S. R., Alzheimer, M., Bremer, B. U. *et al.* Small RNA mediated gradual control of lipopolysaccharide biosynthesis affects antibiotic resistance in Helicobacter pylori. *Nat. Commun.* **12**, 4433 (2021).
17. Hegarty, J. P. & Stewart, D. B. Advances in therapeutic bacterial antisense biotechnology. *Appl. Microbiol. Biotechnol.* **102**, 1055-1065 (2018).

18. Bessa, L. J., Ferreira, M. & Gameiro, P. Evaluation of membrane fluidity of multidrug-resistant isolates of *Escherichia coli* and *Staphylococcus aureus* in presence and absence of antibiotics. *J. Photochem. Photobiol. B.* **181**, 150-156 (2018).
19. Zhang, Y., Ma, W., Ying, Z., *et al.* Inhibiting methicillin-resistant *Staphylococcus aureus* by tetrahedral DNA nanostructure-enabled antisense peptide nucleic acid delivery. *Nano Lett.* **18**, 5652-5659 (2018).
20. van Haasteren, J., Li, J., Scheideler, O.J. *et al.* The delivery challenge: fulfilling the promise of therapeutic genome editing. *Nat. Biotechnol.* **38**, 845–855 (2020).
21. Crooke, S., Wang, S., Vickers, T. *et al.* Cellular uptake and trafficking of antisense oligonucleotides. *Nat. Biotechnol.* **35**, 230–237 (2017).
22. Ho, H., Miu, A., Alexander, M.K. *et al.* Structural basis for dual-mode inhibition of the ABC transporter MsbA. *Nature* **557**, 196–201 (2018).
23. Chen, S., Oldham, M., Davidson, A. *et al.* Carbon catabolite repression of the maltose transporter revealed by X-ray crystallography. *Nature* **499**, 364–368 (2013).
24. Oldham, M. L., Khare, D., Quioco, F. A., Davidson, A. L. & Chen, J. Crystal structure of a catalytic intermediate of the maltose transporter. *Nature* **450**, 515–521 (2007)
25. Oldham, M. L. & Chen, J. Crystal structure of the maltose transporter in a pretranslocation intermediate state. *Science* **332**, 1202–1205 (2011).
26. Gerber, S., Comellas-Bigler, M., Goetz, B. A. & Locher, K. P. Structural basis of trans-inhibition in a molybdate/tungstate ABC transporter. *Science* **321**, 246–250 (2008).
27. Ning, X., Lee, S., Wang, Z. *et al.* Maltodextrin-based imaging probes detect bacteria in vivo with high sensitivity and specificity. *Nat. Mater.* **10**, 602-607 (2011).
28. Zlitni, A., Gowrishankar, G., Steinberg, I. *et al.* Maltotriose-based probes for fluorescence and photoacoustic imaging of bacterial infections. *Nat. Commun.* **11**, 1250 (2020).
29. Tang, J., Chu, B., Wang, J., *et al.* Multifunctional nanoagents for ultrasensitive imaging and photoactive killing of Gram-negative and Gram-positive bacteria. *Nat. Commun.* **10**, 1-14 (2019).
30. Bordignon, E., Grote, M. & Schneider, E. The maltose ATP-binding cassette transporter in the 21st century-towards a structural dynamic perspective on its mode of action. *Mol. Microbiol.* **77**, 1354-1366 (2010).
31. Klebba, P. E. Mechanism of maltodextrin transport through LamB. *Res. Microbiol.* **153**, 417-424 (2002).
32. Charbit, A. Maltodextrin transport through LamB. *Front. Biosci.* **8**, s265-274 (2003).

33. Dippel, R., Boos, W. The maltodextrin system of *Escherichia coli*: metabolism and transport. *J. Bacteriol.* **187**, 8322-8331 (2005).
34. Schonert, S., Seitz, S., Krafft, H. *et al.* Maltose and maltodextrin utilization by *Bacillus subtilis*. *J. Bacteriol.* **188**, 3911-3922 (2006).
35. Prince, J. P., Bolla, J. R., Fisher, G. L. M., *et al.* Acyl carrier protein is essential for MukBEF action in *Escherichia coli* chromosome organization-segregation. *Nat. Commun.* **12**, 6721 (2021).
36. Chen, A., Re, R. N. & Burkart, M. D. Type II fatty acid and polyketide synthases: deciphering protein–protein and protein-substrate interactions. *Nat. Prod. Rep.* **35**, 1029-1045 (2018).
37. Li, G. W., Burkhardt, D., Gross, C., *et al.* Quantifying absolute protein synthesis rates reveals principles underlying allocation of cellular resources. *Cell* **157**, 624–635 (2014).
38. Dryselius, R., Nekhotiaeva, N., Nielsen, P. E., *et al.* Antibiotic-free bacterial strain selection using antisense peptide nucleic acid. *Biotechniques* **35**, 1060-1064 (2003).
39. Nekhotiaeva, N., Awasthi, S. K., Nielsen, P. E., *et al.* Inhibition of *Staphylococcus aureus* gene expression and growth using antisense peptide nucleic acids. *Mol. Ther.* **10**, 652-659 (2004).
40. Järver, P., Coursindel, T., Andaloussi, S. E., *et al.* Peptide-mediated cell and in vivo delivery of antisense oligonucleotides and siRNA. *Mol. Ther. Nucleic Acids.* **1**, e27 (2012).
41. Patenge, N., Pappesch, R., Krawack, F., *et al.* Inhibition of growth and gene expression by PNA-peptide conjugates in *Streptococcus pyogenes*. *Mol. Ther. Nucleic Acids.* **2**, e132 (2013).
42. Leary, S. C. *et al.* Chronic treatment with azide *in situ* leads to an irreversible loss of cytochrome C oxidase activity via holoenzyme dissociation. *J. Biol. Chem.* **277**, 11321–11328 (2002).
43. Kim, Y. C., Shin, M. D., Hackett, S. F. *et al.* Gelling hypotonic polymer solution for extended topical drug delivery to the eye. *Nat. Biomed. Eng.* **4**, 1053-1062 (2020).
44. Weng, Y. H., Ma, X. W., Che, J. *et al.* Nanomicelle-assisted targeted ocular delivery with enhanced antiinflammatory efficacy *in vivo*. *Adv. Sci.* **5**, 1700455 (2018).
45. Seah, I., Loh, X. J. & Su, X. A topical gel for extended ocular drug release. *Nat. Biomed. Eng.* **4**, 1024-1025 (2020).
46. Ch'ng, J. H., Chong, K. K. L., Lam, L. N. *et al.* Biofilm-associated infection by enterococci. *Nat. Rev. Microbiol.* **17**, 82–94 (2019).
47. Bourdeau, R., Lee-Gosselin, A., Lakshmanan, A. *et al.* Acoustic reporter genes for noninvasive imaging of microorganisms in mammalian hosts. *Nature* **553**, 86–90 (2018).

Figures

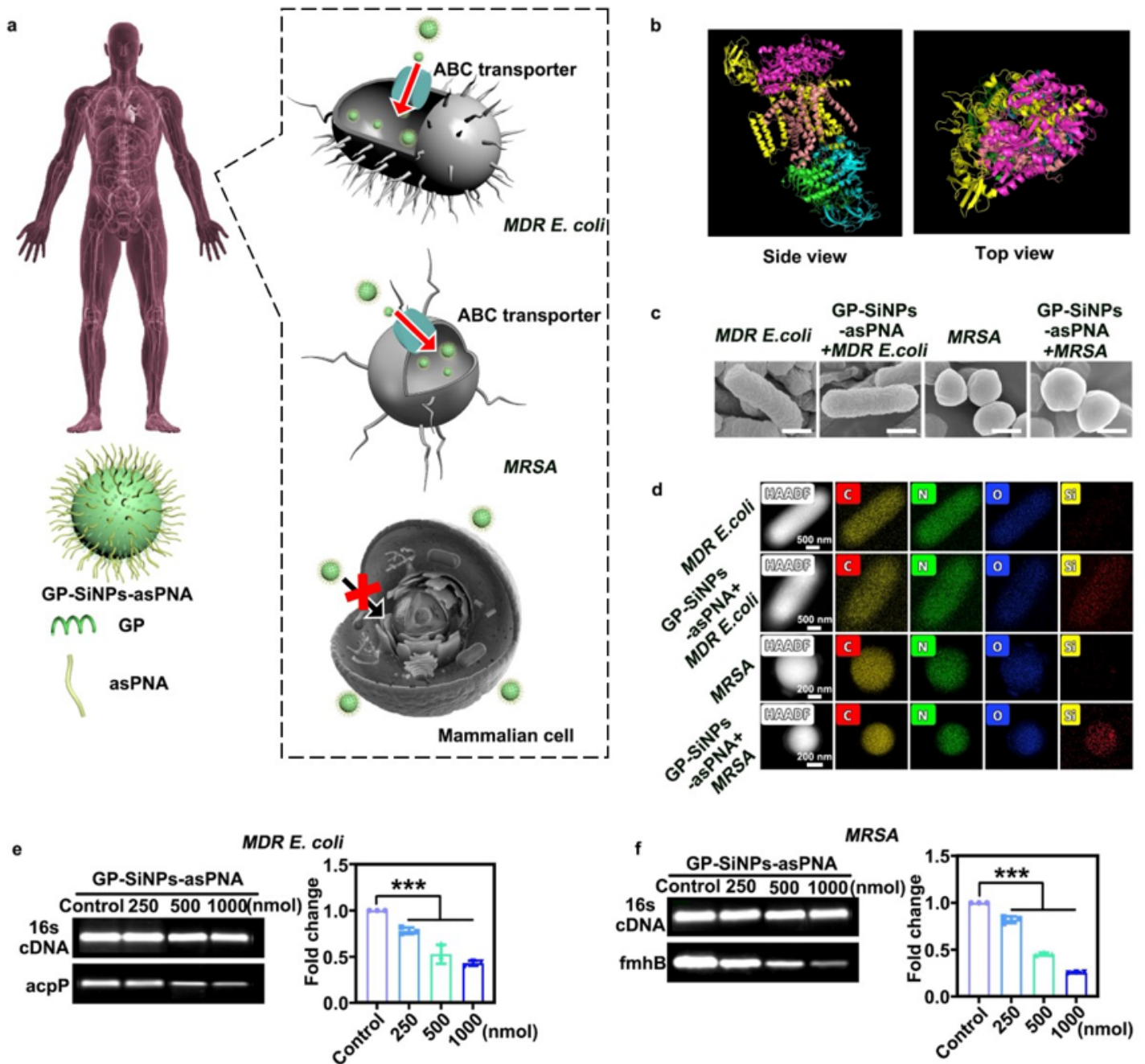


Figure 1

Schematic of the selective delivery of antisense peptide nucleic acids (asPNA) into bacterial cells. **a**, Scheme illustrating the selective internalization of GP-SiNPs-asPNA into human-derived MDR *E. coli* and MRSA cells rather than mammalian cells through the bacteria-specific ABC transporter pathway. The GP-SiNPs-asPNA are made of glucose polymer (GP) (e.g., *poly[4-O-(α -D-glucopyranosyl)-D-glucopyranose]*) and asPNA-modified fluorescent silicon nanoparticles (SiNPs). **b**, The side view and the top view of the structure of ABC transporters in *E. coli*. The structure was simulated by PyMOL software based on the sequences obtained from <http://www.rcsb.org/>. **c**, SEM images of MDR *E. coli*, MDR *E. coli* treated with

GP-SiNPs-asPNA (MDR *E. coli* + GP-SiNPs-asPNA), MRSA and MRSA treated with GP-SiNPs-asPNA (MRSA + GP-SiNPs-asPNA). Scale bars: 500 nm. **e**, Elemental mapping in HAADF-STEM images of MDR *E. coli*, MDR *E. coli* + GP-SiNPs-asPNA, MRSA and MRSA + GP-SiNPs-asPNA. MDR *E. coli* or MRSA were incubated with GP-SiNPs-asPNA at 37 °C for 2 h. After incubation, the treated bacteria were rinsed with PBS buffer several times. The bacterial cell concentration was $\sim 1.0 \times 10^7$ CFU. **e**, Semiquantitative analysis of gel electrophoresis of *acpP* gene expression and corresponding quantitative real-time PCR analysis. The *acpP* gene was extracted from MDR *E. coli* upon exposure to different concentrations of GP-SiNPs-asPNA. **f**, Semiquantitative analysis of gel electrophoresis of *fmhB* gene expression and corresponding quantitative real-time PCR analysis. The *fmhB* gene was extracted from MRSA upon exposure to different concentrations of GP-SiNPs-asPNA. Statistical analysis was performed using one-way ANOVA. Error bars represent the standard deviation obtained from three independent measurements (***) means $p < 0.001$, $n = 3$).

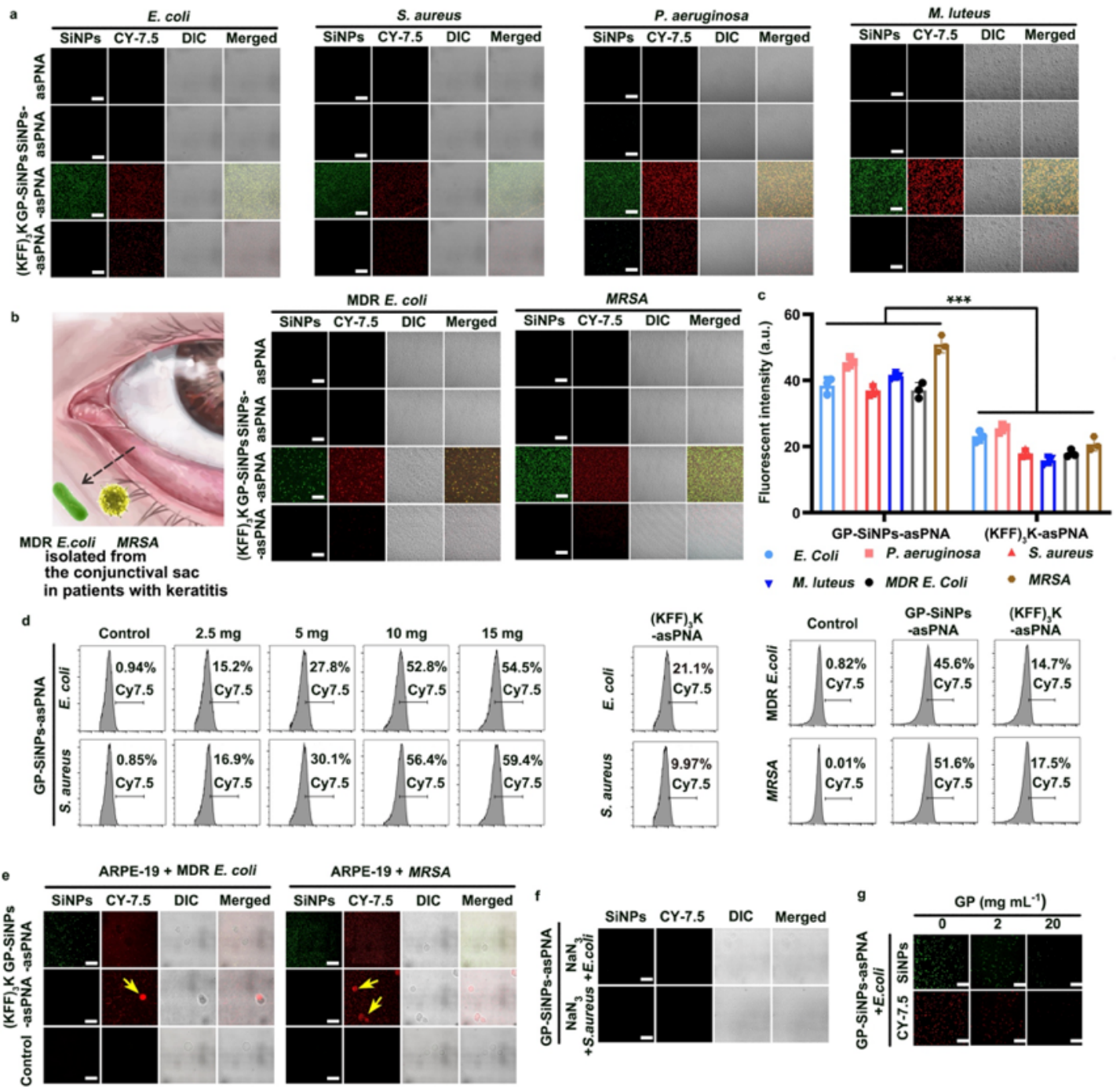


Figure 2

The hitchhiking strategy for *in vitro* imaging of diverse bacteria. **a**, Confocal fluorescence images of bacteria (e.g., *E. coli*, *S. aureus*, *P. aeruginosa*, *M. luteus*) after incubation with asPNA, SiNPs-asPNA, GP-SiNPs-asPNA and (KFF)₃K-asPNA (Cy7.5 labeled) with the equivalent dose at 37 °C for 2 h, followed by washing with PBS buffer several times. **b**, Confocal fluorescence images of human-derived strains (e.g., MRSA and MDR *E. coli*) isolated from the conjunctival sac in patients with keratitis after the same treatments. **c**, Corresponding histograms of fluorescent intensity (***) means $p < 0.001$, $n=3$). **d**, Flow cytometry analysis of the uptake rates of GP-SiNPs-asPNA or (KFF)₃K-asPNA by *E. coli*, *S. aureus*, MDR *E.*

coli and *MRSA*. The amount of linked GP is 2.5, 5, 10 or 15 mg mL⁻¹. GP-SiNPs-asPNA and (KFF)₃K-asPNA are loaded with the same amount of asPNA (e.g., 1 μM). **e**, Confocal fluorescence images of the mixture of ARPE-19 and MDR *E. coli* (ARPE-19 + MDR *E. coli*, Control), (ARPE-19 + MDR *E. coli*) treated with GP-SiNPs-asPNA, (ARPE-19 + MDR *E. coli*) treated with (KFF)₃K-asPNA, and confocal fluorescence images of the mixture of ARPE-19 and *MRSA* (ARPE-19 + *MRSA*, Control), (ARPE-19 + *MRSA*) treated with GP-SiNPs-asPNA, (ARPE-19 + *MRSA*) treated with (KFF)₃K-asPNA. Scale bars: 10 μm. Yellow arrows indicate ARPE-19 cells. **f**, Confocal fluorescence images of *E. coli* or *S. aureus* treated with NaN₃ and then incubated with GP-SiNPs-asPNA for 2 h. Scale bars: 10 μm. **g**, Confocal fluorescence images of *E. coli* incubated with GPs at different concentrations (0, 2, 20 mg mL⁻¹) for 5 min and then incubated with GP-SiNPs-asPNA for 2 h. Scale bars: 10 μm. The bacterial cell concentration is ~1.0×10⁷ CFU.

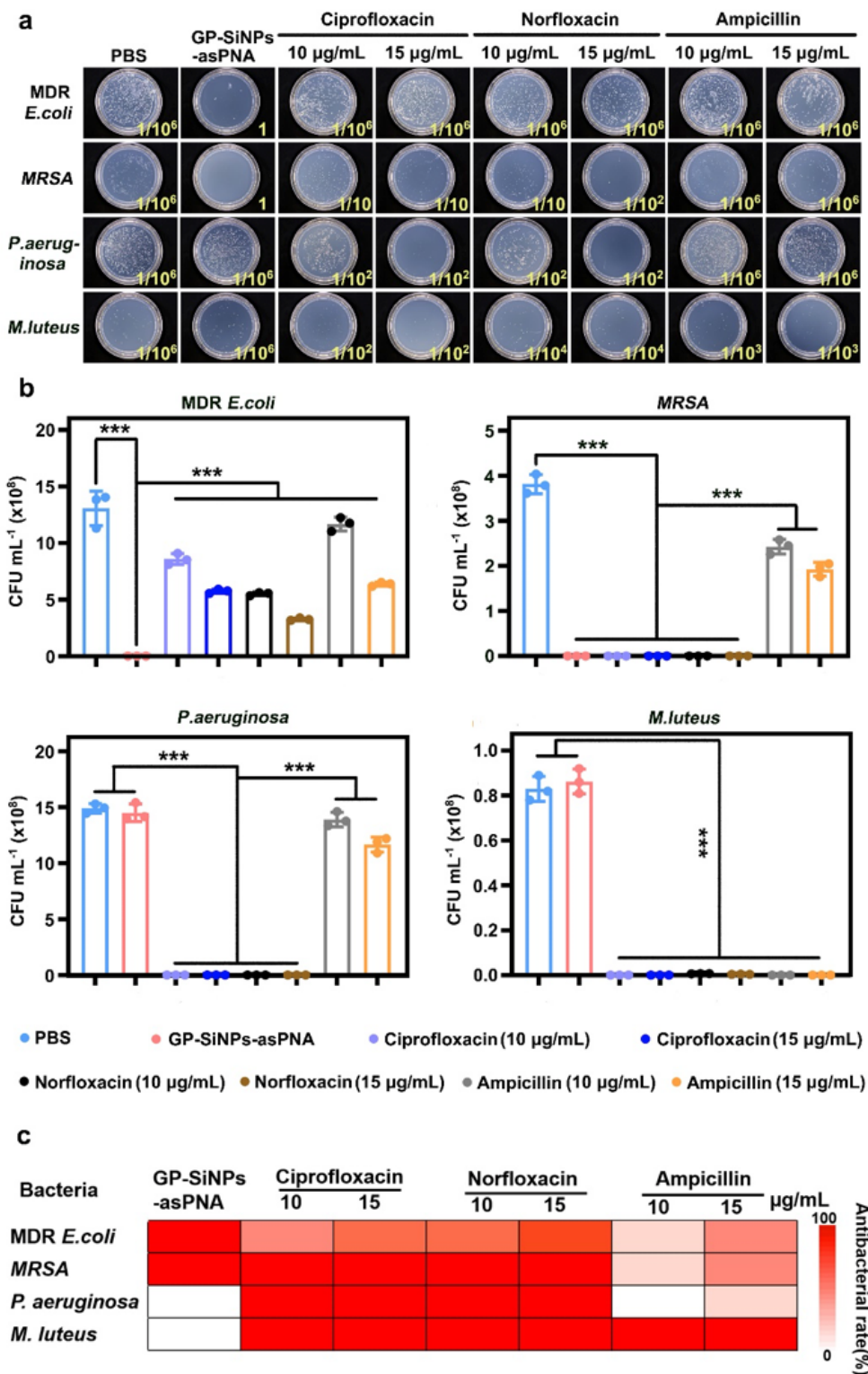


Figure 3

Agar plate assays to evaluate the *in vitro* antimicrobial activity of the developed strategy. **a**, Photographs of agar plates of MDR *E. Coli*, MRSA, *P. aeruginosa* and *P. aeruginosa* treated by GP-SiNPs-asPNA (1 μM), ciprofloxacin, norfloxacin and ampicillin with various concentrations for 12 h. **b**, Corresponding histograms of bacterial amounts. Statistical analysis was performed using one-way ANOVA. Error bars

represent the standard deviation obtained from three independent measurements (***) means $p < 0.001$, $n=3$). **c**, Corresponding antibacterial rates.

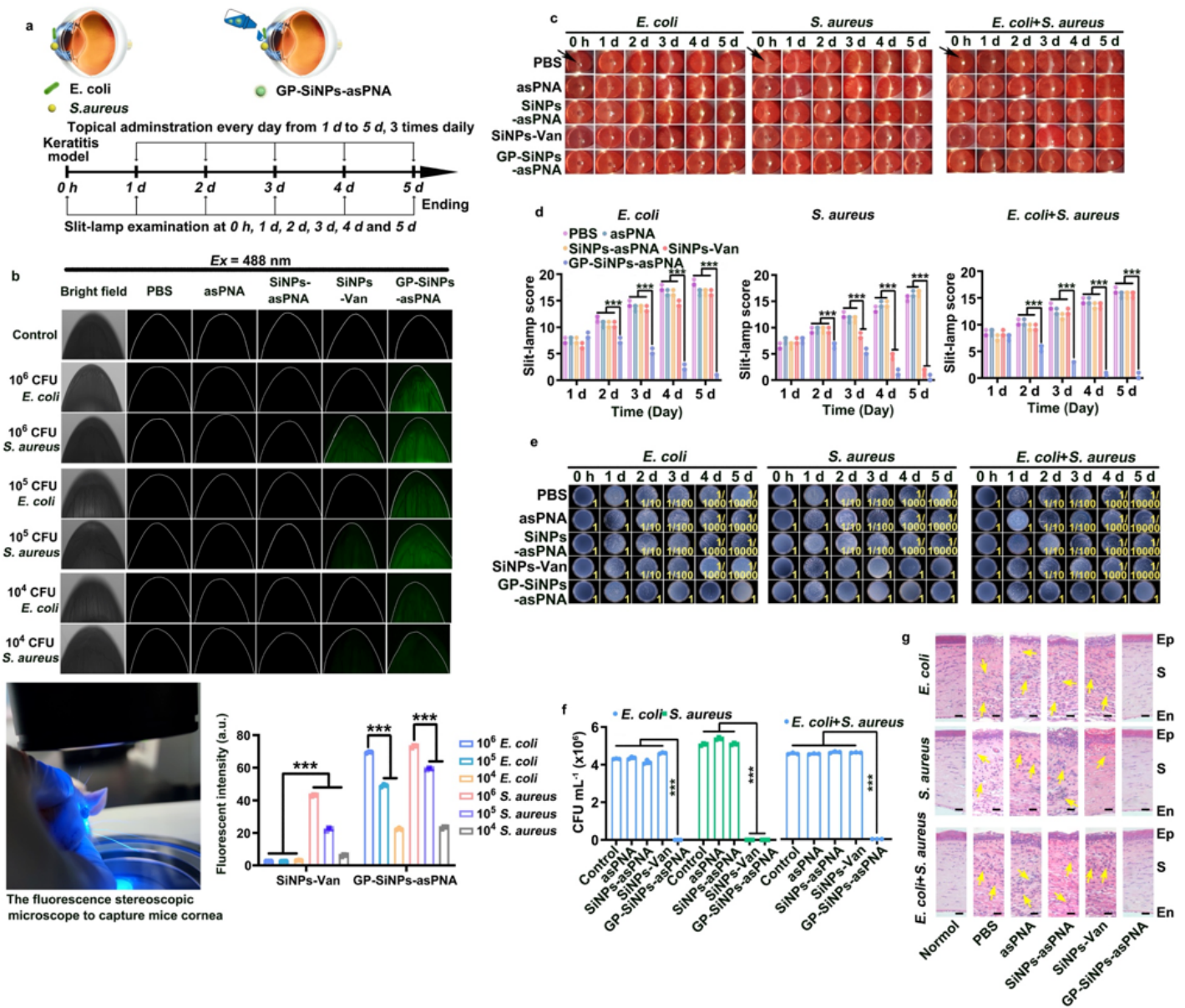


Figure 4

Evaluation of the hitchhiking strategy in the therapy of bacterial keratitis. **a**, Scheme illustrating the construction of the model of bacterial keratitis in mice and the corresponding treatment procedures. **b**, Fluorescent images of bacterial keratitis induced by *E. coli* or *S. aureus* at various concentrations based on the proposed strategy. The infected corneas and healthy corneas were treated with PBS, asPNA (1 μM), SiNPs-asPNA (1 μM), SiNPs-Van (10 mg mL⁻¹) or GP-SiNPs-asPNA (1 μM). The actual count of *E. coli* or *S. aureus* at the infected cornea during imaging was determined by tissue harvesting, homogenization and culturing with CFU count. All imaging experiments were repeated three times with similar results. **c-g**, Daily slit lamp microscopic images of 2.0×10⁸ CFU *E. coli*, *S. aureus* or *E. coli* + *S. aureus*-infected corneas with different treatments (e.g., PBS, asPNA (1 μM), SiNPs-asPNA (1 μM), SiNPs-

Van (10 mg mL^{-1}) or GP-SiNPs-asPNA ($1 \text{ }\mu\text{M}$) (1 drop per time, 3 times per day)) (**c**), corresponding histograms of slit-lamp examination scores (**d**), homogenates of infected corneas with different treatments for 0, 1, 2, 3, 4 and 5 d cultured on solid LB agar ($n=3$) (**e**), corresponding quantification of bacterial colonization (**f**), and H&E staining images of infected corneas with different treatments for 5 d (**g**). Scale bars: $25 \text{ }\mu\text{m}$. The black arrows in slit lamp images indicate the position of the pupil. The yellow arrows in H&E staining indicate granulocyte infiltration. Statistical analysis was performed using one-way ANOVA. Error bars represent the standard deviation obtained from three independent measurements (***) means $p < 0.001$, $n = 3$).

Supplementary Files

This is a list of supplementary files associated with this preprint. Click to download.

- [Reportingsummary.pdf](#)
- [Checklist.pdf](#)
- [NatBiotechnolSupplementinformationfinalversion.docx](#)